



Available online at www.sciencedirect.com

SciVerse ScienceDirect

Nuclear Physics A 900 (2013) 51–64

NUCLEAR
PHYSICS

A

www.elsevier.com/locate/nuclphysa

New insights into antikaon–nucleon scattering and the structure of the $\Lambda(1405)$

Maxim Mai ^{a,*}, Ulf-G. Meißner ^{a,b}

^a Universität Bonn, Helmholtz-Institut für Strahlen- und Kernphysik (Theorie),
and Bethe Center for Theoretical Physics, D-53115 Bonn, Germany

^b Forschungszentrum Jülich, Institut für Kernphysik, Institute for Advanced Simulation,
and Jülich Center for Hadron Physics, D-52425 Jülich, Germany

Received 6 November 2012; received in revised form 23 January 2013; accepted 24 January 2013

Available online 30 January 2013

Abstract

We perform a combined analysis of antikaon–nucleon scattering cross sections and the recent SID-DHARTA kaonic hydrogen data in the framework of a $\bar{K}N-\pi Y$ coupled-channel Bethe–Salpeter approach at next-to-leading order in the chiral expansion of the effective potential. We find a precise description of the antikaon–proton scattering amplitudes and are able to extract accurate values of the scattering lengths, $a_0 = -1.81^{+0.30}_{-0.28} + i0.92^{+0.29}_{-0.23}$ fm and $a_1 = +0.48^{+0.12}_{-0.11} + i0.87^{+0.26}_{-0.20}$ fm. We also discuss the two-pole structure of the $\Lambda(1405)$.

© 2013 Elsevier B.V. All rights reserved.

Keywords: Kaon–baryon interactions; Baryon resonances

1. Introduction and summary

With the recent precise measurement of the characteristics of kaonic hydrogen by the SID-DHARTA collaboration [1], an accurate determination of the so important antikaon–nucleon scattering amplitude is now possible. The appropriate framework to perform this task is unitarized chiral perturbation theory, which combines the strictures from the chiral SU(3) dynamics of QCD with coupled channel effects, that e.g. generate the much discussed $\Lambda(1405)$ resonance, as first pointed out by Dalitz and Tuan [2]. From earlier studies by various groups, it is already

* Corresponding author.

E-mail address: mai@hiskp.uni-bonn.de (M. Mai).

known that simply taking the leading order chiral interactions in the effective potential of the respective scattering equation is insufficient to achieve the desired accurate theoretical description, see e.g. Refs. [3–5]. In fact, Ikeda et al. [6,7] have performed such a combined analysis based on the next-to-leading order (NLO) chiral effective meson–baryon Lagrangian, nicely demonstrating that indeed a more precise description of the $K^- p$ and $K^- n$ interaction arises (see also Ref. [8]). Here, we perform a similar analysis, but in contrast to Refs. [6,7], we use a Bethe–Salpeter framework without an on-shell approximation for the intermediate meson–baryon states (as described in more detail below). The framework we use has already been successfully applied to pion–nucleon scattering in the s-waves [9] as well as s-wave pion photoproduction [10] and thus it is natural to extend this analysis to antikaon–nucleon scattering. We also point out that the constraints from SIDDHARTA on the kaon–deuteron scattering length have been investigated in [11] (see also [12]).

The main results of our investigation can be summarized as follows:

- Fitting the scattering data for $K^- p \rightarrow K^- p, \bar{K}^0 n, \Sigma^\pm \pi^\mp$, and $\Sigma^0 \pi^0$ for laboratory momenta $p_{\text{lab}} \leq 300$ MeV together with the SIDDHARTA data allows for a good description of the antikaon–proton cross section data (cf. Fig. 1) and an accurate determination of the scattering lengths, cf. Eq. (7).
- We can give a precise prediction for the real and imaginary part of the s-wave $K^- p \rightarrow K^- p$ scattering amplitude f_{0+} for center-of-mass energies $1330 \leq W_{\text{cms}} \leq 1450$ MeV, cf. Fig. 4. We note that the subthreshold amplitude differs from the one of Ikeda et al. [6,7] although the scattering and bound state data are equally well described in both approaches.
- We have investigated the two-pole structure of the $\Lambda(1405)$ [13,14]. While the first pole is in agreement with other determinations, we find the real part of the second pole at larger energies than usually obtained. We trace this back to the contributions from the NLO terms in the driving potential. In contrast to most other works we neither restrict those to be small nor perform an s-wave projection of the kernel.
- We determine the coupling of both isospin $I = 0$ poles to the $\bar{K}N$ and $\pi\Sigma$ channels. We observe a nice qualitative agreement with the observation made in Refs. [4,14].

The manuscript is organized as follows: In Section 2 we discuss the underlying Bethe–Salpeter framework. In particular, we spell out clearly the approximation we make to solve the BSE and the differences to the on-shell approach, frequently used in the literature. Moreover, we present a new method to deal with ‘unphysical’ poles that often arise in such coupled-channel investigations. Section 3 describes our fit strategy, whereas our results are presented and discussed in Section 4. The appendix contains the relevant couplings for the meson–baryon scattering processes.

2. Framework

The starting point of our work is the recent analysis of πN scattering, presented in Ref. [9]. In this section we describe the basic ingredients of this approach.

In chiral perturbation theory the meson–baryon interaction at the leading chiral order is encoded in the following Lagrangian

$$\mathcal{L}_{\phi B}^{(1)} = \langle \bar{B} (i\gamma_\mu D^\mu - m_0) B \rangle + \frac{D}{2} \langle \bar{B} \gamma_\mu \gamma_5 [u^\mu, B]_+ \rangle + \frac{F}{2} \langle \bar{B} \gamma_\mu \gamma_5 [u^\mu, B] \rangle, \quad (1)$$

where $\langle \dots \rangle$ denotes the trace in flavor space, $D_\mu B := \partial_\mu B + \frac{1}{2}[[u^\dagger, \partial_\mu u], B]$, m_0 is the baryon octet mass in the chiral SU(3) limit, and D, F are the axial coupling constants. The relevant degrees of freedom are the Goldstone bosons (π, K, η) and the low-lying baryons (N, Λ, Σ, Ξ). The Goldstone bosons are described by the traceless meson matrix ϕ , which is included in the above Lagrangian via $u^2 := \exp(i\phi/F_0)$ and $u^\mu := iu^\dagger \partial^\mu u - iu \partial^\mu u^\dagger$. Here, F_0 is the meson decay constant in the chiral limit. The low-lying baryons are collected in the traceless matrix B . We set the external currents to zero except for the scalar one, which is set equal to the quark mass matrix, i.e. $s = \mathcal{M} := \text{diag}(m_u, m_d, m_s)$. We furthermore use $\chi_\pm := u^\dagger \chi u^\dagger \pm u \chi^\dagger u$ and $\chi := 2B_0 s$, where the constant B_0 is related to the quark condensate in the chiral limit. For more details on our conventions and definitions, we refer to Ref. [9].

Starting from the covariant derivative $D_\mu B$, the so-called Weinberg–Tomozawa term can be derived. This term dominates the s-wave interaction near the thresholds, therefore in most early chiral unitary approaches the meson–baryon interaction was restricted to this term. Secondly, a meson can couple to a baryon via the axial vector current $\sim D, F$, generating the s- and u-channel exchanges of the intermediate baryons. The inclusion of these so-called Born graphs in the driving term of the Bethe–Salpeter equation leads to conceptual and practical difficulties, which are described in detail in Refs. [9,10]. The latter are usually overcome, making use of the on-shell approximation or via projection of the kernel to the s-wave, see e.g. Ref. [5] and Ref. [6] for a more recent study. However, the particular attention of the present work lies on the solution of the Bethe–Salpeter equation with the full off-shell dependence. Thus we will restrict the interaction kernel to a sum of contact terms, but refrain from the approximations mentioned above. Aside from the Weinberg–Tomozawa term, we will take into account the full set of meson–baryon vertices from the second-order chiral Lagrangian. The pertinent Lagrangian density was first constructed in Ref. [15] and reads in its minimal form [16]

$$\begin{aligned} \mathcal{L}_{\phi B}^{(2)} = & b_{D/F} \langle \bar{B}[\chi_+, B]_\pm \rangle + b_0 \langle \bar{B}B \rangle \langle \chi_+ \rangle + b_{1/2} \langle \bar{B}[u_\mu, [u^\mu, B]]_\mp \rangle \\ & + b_3 \langle \bar{B}\{u_\mu, \{u^\mu, B\}\} \rangle + b_4 \langle \bar{B}B \rangle \langle u_\mu u^\mu \rangle \\ & + ib_5 \langle \bar{B}\sigma^{\mu\nu} [[u_\mu, u_\nu], B] \rangle + ib_6 \langle \bar{B}\sigma^{\mu\nu} [[u_\mu, u_\nu], B]_+ \rangle + ib_7 \langle \bar{B}\sigma^{\mu\nu} u_\mu \rangle \langle u_\nu B \rangle \\ & + \frac{ib_{8/9}}{2m_0} (\langle \bar{B}\gamma^\mu [u_\mu, [u_\nu, [D^\nu, B]]_\mp] \rangle + \langle \bar{B}\gamma^\mu [D_\nu, [u^\nu, [u_\mu, B]]_\mp] \rangle) \\ & + \frac{ib_{10}}{2m_0} (\langle \bar{B}\gamma^\mu \{u_\mu, \{u_\nu, [D^\nu, B]\}\} \rangle + \langle \bar{B}\gamma^\mu [D_\nu, \{u^\nu, \{u_\mu, B\}\}] \rangle) \\ & + \frac{ib_{11}}{2m_0} (2\langle \bar{B}\gamma^\mu [D_\nu, B] \rangle \langle u_\mu u^\nu \rangle + \langle \bar{B}\gamma^\mu B \rangle \langle [D_\nu, u_\mu] u^\nu + u_\mu [D_\nu, u^\nu] \rangle), \end{aligned} \quad (2)$$

with the b_i the pertinent dimension-two low energy constants (LECs). The LECs $b_{0,D,F}$ are the so-called *symmetry breakers*, while the b_i ($i = 1, \dots, 11$) are referred to as *dynamical* LECs. Note that such terms may lead to sizable corrections to the leading-order result, see e.g. Refs. [17, 18] for the calculation of meson–baryon scattering lengths up to the third chiral order. Clearly, when fitting the LECs to data, some effects of the omitted Born graphs will be taken into account through these higher-order local terms.

Consider now the scattering process $\phi(q_1)B(p_1) \rightarrow \phi(q_2)B(p_2)$. Let us denote the in- and out-going meson momenta by q_1 and q_2 , respectively. The overall four-momentum is given by $p = q_1 + p_1 = q_2 + p_2$, where p_1 and p_2 are the momenta of in- and out-going baryon, respectively. Separating the momentum space from the channel space structures, the chiral potential considered here takes the form:

$$V(\not{q}_2, \not{q}_1; p) = A_{WT}(\not{q}_1 + \not{q}_2) + A_{14}(q_1 \cdot q_2) + A_{57}[\not{q}_1, \not{q}_2] + A_M \\ + A_{811}(\not{q}_2(q_1 \cdot p) + \not{q}_1(q_2 \cdot p)),$$

where the first matrix A_{WT} only depends on the meson decay constants $F_{\pi,K}$, whereas A_{14} , A_{57} , A_{811} and A_M also contain the NLO LECs as specified in [Appendix A](#). In going from the Lagrangian (2) to the above vertex rule, we have left out some terms, which are formally of third chiral order (but only start contributing at fourth order, i.e. beyond the accuracy considered here). The channel space is defined in accordance with the quantum numbers as well as the energy range of interest. For the purpose of gaining some insight on the nature of $\Lambda(1405)$ it is spanned by six vectors corresponding to the following meson–baryon states: $\{K^- p; \bar{K}^0 n; \pi^0 \Lambda; \pi^0 \Sigma^0; \pi^+ \Sigma^-; \pi^- \Sigma^+\}$. The influence of other much heavier channels will be absorbed in the LECs to be fitted.

The strict perturbative chiral expansion is only applicable at low energies and certainly fails in the vicinity of (subthreshold) resonances (for a nice demonstration see e.g. [19].) We extend the range of applicability by means of a coupled channel Bethe–Salpeter equation (BSE). Introduced in Ref. [20] it has been proven to be very useful both in the purely mesonic and also in the meson–baryon sector. In contrast to perturbative calculations this approach implements two-body unitarity exactly and in principle allows to generate resonances dynamically. For the meson–baryon scattering amplitude $T(\not{q}_2, \not{q}_1; p)$ and the chiral potential $V(\not{q}_2, \not{q}_1; p)$ the integral equation to be solved reads

$$T(\not{q}_2, \not{q}_1; p) = V(\not{q}_2, \not{q}_1; p) + i \int \frac{d^d l}{(2\pi)^d} V(\not{q}_2, \not{l}; p) S(\not{p} - \not{l}) \Delta(l) T(\not{l}, \not{q}_1; p), \quad (3)$$

where S and Δ represent the baryon (of mass M) and the meson (of mass m) propagator, respectively, and are given by $iS(\not{p}) = i/(\not{p} - m + i\epsilon)$ and $i\Delta(k) = i/(k^2 - M^2 + i\epsilon)$. Moreover, T , V , S and Δ in the last expression are matrices in the channel space. To treat the loop diagrams appearing in the BSE (3), we utilize dimensional regularization. The purely baryonic integrals are set to zero from the beginning. In the spirit of our previous work [9], we apply the usual $\overline{\text{MS}}$ subtraction scheme, keeping in mind that the modified loop integrals are still scale-dependent. The scale μ reflects the influence of the higher-order terms not included in our potential. It is used as a fitting parameter of our approach.

The solution of the BSE (3) with full off-shell dependence is obtained following the construction principles described in Ref. [9]. However, before proceeding with this solution, we wish to address another very important issue, namely the presence of ‘unphysical’ poles on the physical Riemann sheet. As a matter of fact, the BSE ansatz is known to produce such poles which are forbidden by the postulate of maximal analyticity. It turns out that in the case of pion-nucleon scattering these ‘unphysical’ poles are located very far away from the physical region, such that their influence is completely negligible. However, in the case of the antikaon–nucleon scattering these can appear in the proximity of the physical region. Thus a prescription is required to rule out such unphysical solutions.

The most common method to achieve this is to keep only those solutions of the BSE, which do not produce poles on the first Riemann sheet ‘near’ the real (physical) axis. E.g. in Ref. [5] solutions producing poles for $\text{Im}(W_{\text{cms}} = \sqrt{s}) < 250$ MeV were excluded by hand. To overcome such unsatisfactory intervention into the fitting procedure we continue differently, relying on fundamental properties of holomorphic functions. We start with the one-meson–one-baryon loop-function $I_{MB}(s = p^2)$ in four dimensions.

$$I_{MB}(s) := \int \frac{d^4 l}{(2\pi)^4} \frac{1}{l^2 - M^2} \frac{1}{(p-l)^2 - m^2}.$$

Applying the Cutkosky rules, one immediately obtains the imaginary part of this integral, given by $-q_{\text{cms}}/(8\pi\sqrt{s})$ for $q_{\text{cms}}^2 = (s - (m + M)^2)(s - (m - M)^2)/(4s)$. Keeping in mind the high-energy behavior of the function $I_{MB}(s)$, we can obtain the real part of it via a subtracted dispersion relation

$$\text{Re}(I_{MB}(s)) = \text{Re}(I_{MB}(s_0)) + \frac{(s - s_0)}{\pi} \text{PV} \int_{s_{\text{thr}}}^{\infty} ds' \frac{\text{Im}(I_{MB}(s'))}{(s' - s)(s' - s_0)},$$

where $s_{\text{thr}} = (M + m)^2$ and s_0 is a subtraction point chosen to not lie on the integration contour and ‘PV’ denotes the principal value. The solution of the BSE, Eq. (3), corresponds to a bubble sum, containing exactly the same one loop-functions I_{MB} . Thus one might, in principle, be able to write an equation similar to the last one for the scattering amplitude

$$\text{Re}(T(s)) = \text{Re}(T(s_0)) + \frac{(s - s_0)}{\pi} \text{PV} \int_{s_{\text{thr}}}^{\infty} ds' \frac{\text{Im}(T(s'))}{(s' - s)(s' - s_0)}, \quad (4)$$

where for the moment we have suppressed the \not{q}_1 and \not{q}_2 dependence. To the best of our knowledge, it is not possible to implement the last relation (4) into the BSE (3) directly. This is actually the reason for the presence of the ‘unphysical’ poles. Nevertheless, the last equation can be of enormous use to quantify the influence of these poles on the physical axis. To put this in other words, the difference between the left- and right-hand sides of this equation will become smaller if the poles are located far away from the real axis and vice versa. Hence, minimizing this difference we can constrain the parameter space in a rather systematic way to physically meaningful solutions.

More specifically, to find the solution which agrees with experimental input without producing ‘unphysical’ poles, we simply minimize the following quantity $\chi_{\text{FULL}}^2 = \chi_{\text{DISP}}^2 + \chi_{\text{DATA}}^2$, with χ_{DATA}^2 reflecting the goodness of the description of the experimental data and

$$\chi_{\text{DISP}}^2 = \left(1 - \frac{(s - s_0)}{\pi} \frac{\text{PV} \int_{s_{\text{thr}}}^{\infty} ds' \frac{\text{Im}(T(s'))}{(s' - s)(s' - s_0)}}{\text{Re}(T(s) - T(s_0))} \right)^2. \quad (5)$$

It should be clear that the present choice of χ_{DISP}^2 is by no means unique. However, it seems to be the most natural choice as it amounts to a simple algebraic manipulation of Eq. (4). We have checked numerically that the absolute value of scattering amplitude T has the correct high-energy behavior and thus the integral in the above equation is well defined. For the subtraction point we have chosen $\sqrt{s_0} = 0.6$ GeV which certainly lies within the integration contour,¹ and, for technical reasons, χ_{DISP}^2 is calculated for several distinct values of s along the physically relevant region, i.e. $\sqrt{s} \sim 1.3\text{--}1.7$ GeV. Indeed, we see that parameter sets which minimize the χ_{DISP}^2 correspond to the solution of the BSE with no physical poles in the proximity of the real axis. Thus, while the exact restoration of analyticity is a more complicated issue, we can use the above procedure for our more practical purpose, namely to simply rule out the ‘unphysical’ solutions of the BSE.

¹ We note that none of the results presented later depends on the choice of the actual value of s_0 as long as it chosen within the integration contour and commensurate with underlying scales in the problem at hand.

3. Fit strategy

We are now able to confront our approach with the experimental results. Throughout the present work we use the following numerical values (in GeV) for the masses and the meson decay constants: $F_\pi = 0.0924$, $F_K = 0.113$, $M_{\pi^0} = 0.135$, $M_{\pi^\pm} = 0.1396$, $M_{K^-} = 0.4937$, $M_{\bar{K}^0} = 0.4977$, $m_p = 0.9383$, $m_n = 0.9396$, $m_\Lambda = 1.1157$, $m_{\Sigma^0} = 1.1926$, $m_{\Sigma^+} = 1.1894$ and $m_{\Sigma^-} = 1.1975$. The baryon mass in the chiral limit, m_0 in Eq. (2), can be fixed to 1 GeV without loss of generality, as any other value only amounts to a rescaling of some of the unknown LECs.

Secondly, for the experimental data we consider total cross sections for the processes $K^- p \rightarrow \{K^- p, \bar{K}^0 n, \pi^0 \Sigma^0, \pi^+ \Sigma^-, \pi^- \Sigma^+\}$ taken from Refs. [21–24]. Moreover, we consider the following decay ratios

$$\gamma = \frac{\Gamma(K^- p \rightarrow \pi^+ \Sigma^-)}{\Gamma(K^- p \rightarrow \pi^- \Sigma^+)} = 2.38 \pm 0.04,$$

$$R_n = \frac{\Gamma(K^- p \rightarrow \pi^0 \Lambda)}{\Gamma(K^- p \rightarrow \text{neutral states})} = 0.189 \pm 0.015,$$

$$R_c = \frac{\Gamma(K^- p \rightarrow \pi^+ \Sigma^-, \pi^- \Sigma^+)}{\Gamma(K^- p \rightarrow \text{inelastic channels})} = 0.664 \pm 0.011,$$

where the first one is taken from Ref. [25] and the last two from Ref. [26]. Additionally to these quite old data, we use a recent determination of the energy shift and width of the kaonic hydrogen in the 1s state, i.e. $\Delta E - i\Gamma/2 = (283 \pm 42) - i(271 \pm 55)$ eV from the SIDDHARTA experiment at DAΦNE [1]. These are related to the $K^- p$ scattering length via the modified Deser-type relation [28]

$$\Delta E - i\Gamma/2 = -2\alpha^3 \mu_c^2 a_{K^- p} [1 - 2a_{K^- p} \alpha \mu_c (\ln \alpha - 1)],$$

where $\alpha \simeq 1/137$ is the fine-structure constant, μ_c is the reduced mass and $a_{K^- p}$ the scattering length of the $K^- p$ system. It should be noted that the threshold ratio γ was measured in [26] in large disagreement to the results presented in [27]. Thus, the error bars are enhanced in the fitting routine by the factor of ten effectively weighting the old threshold data equally to the recent experimental data from the SIDDHARTA experiment.

There are 17 free parameters in the present approach. First of all, the low-energy constants represent the heavy degrees of freedom of QCD, which are integrated out. Thus they have to be fixed in a fit to the experimental data. As a matter of fact, the fitting parameters of our approach correspond to the SU(3) low-energy constants, renormalized by the effects of the not included channels $\{\eta\Lambda; \eta\Sigma^0; K^+\Xi^-; K^0\Xi^0\}$. Additionally, three subtraction constants have to be determined from a fit, which correspond to the logarithms of the undetermined regularization scales $\{\mu_{\pi\Lambda}, \mu_{KN}, \mu_{\pi\Sigma}\}$.

To reproduce the experimental data as well as to preserve the property of analyticity as described above, we minimize the following quantity $\chi^2_{\text{FULL}} = \chi^2_{\text{DISP}} + \chi^2_{\text{DATA}}$, where the first part is given in Eq. (5) and the second part by the quantity

$$\chi^2_{\text{DATA}} := \frac{\chi^2}{\text{d.o.f.}} = \frac{\sum_i n_i}{N(\sum_i n_i - p)} \sum_i \frac{\chi_i^2}{n_i}.$$

Here, p is the number of the free parameters, n_i is the number of data points available for the observable i and N is the number of observables. The present choice of χ^2_{DATA} is crucial to

ensure the equal weight of different observables, independently of the corresponding number of data points. The minimization itself is performed using MINUIT [29], especially the migrad strategy in two steps, which is due to the quite complicated structure of the BSE solution with full off-shell dependence. First, parameters are found to minimize the χ^2_{FULL} in the on-shell approximation. In the second step we turn on the “off-shellness” slowly, minimizing in each step the χ^2_{DATA} and taking the parameters of the best fit from the previous step as starting values. Such a procedure guarantees preservation of the right analytic properties of the solution, found in the first step.

4. Results

For the best fit, i.e. $\chi^2_{\text{DATA, BEST}} = 0.524$, we obtain the following parameter set (all b_i in GeV^{-1} and μ_i in GeV)

$$\begin{aligned}\log(\mu_{KN}/(1 \text{ GeV})) &= +1.155 \pm 0.181, \\ \log(\mu_{\pi\Sigma}/(1 \text{ GeV})) &= -0.008 \pm 0.002, \\ \log(\mu_{\pi\Lambda}/(1 \text{ GeV})) &= -0.010 \pm 0.003, \\ b_0 &= +0.710 \pm 0.211, & b_D &= -0.291 \pm 0.068, & b_F &= -0.057 \pm 0.014, \\ b_1 &= +0.582 \pm 0.052, & b_2 &= -0.310 \pm 0.092, & b_3 &= +0.227 \pm 0.038, \\ b_4 &= -0.939 \pm 0.069, & b_5 &= +0.023 \pm 0.007, & b_6 &= +0.001 \pm 0.001, \\ b_7 &= -2.518 \pm 0.110, & b_8 &= -0.332 \pm 0.045, & b_9 &= +0.298 \pm 0.087, \\ b_{10} &= +0.198 \pm 0.058, & b_{11} &= +0.516 \pm 0.058.\end{aligned}$$

We note that the LECs are all of natural size ($\mu_{KN} = 3.17 \text{ GeV}$, $\mu_{\pi\Sigma} = 0.99 \text{ GeV}$, $\mu_{\pi\Lambda} = 0.99 \text{ GeV}$), indicating that all relevant physical mechanisms are included in the calculations. The experimental data on total cross sections is reproduced quite nicely, see Fig. 1. We first wish to remark that due to insufficient number of data points the channel $K^- p \rightarrow \Lambda \pi^0$ is not considered as experimental input in the fit procedure. For completeness, we present the outcome of our approach for this channel also in Fig. 1. Secondly, all of the cross sections presented here are due to the strong interaction only. Additionally, Coulomb interaction was taken into account in [5,7] via a non-relativistic quantum mechanical formula. Since this alone cannot count for an interference between the strong and the electromagnetic interactions, we relegate the proper inclusion of the electromagnetic contributions to a future publication.

The confidence bands presented in the above figure and the errors on further observables are calculated as follows: first we generate a large number ($\sim 10,000$) of randomly distributed parameter sets in the error region given above. Then for each of these parameter sets we calculate the χ^2_{DATA} and keep only those sets, for which $\chi^2_{\text{DATA}} - \chi^2_{\text{DATA, BEST}} \leq 1.05$. Quantities calculated for these parameter sets are assumed to lie in the 1σ region around the central value. For a more detailed description of this procedure, see Ref. [5].

The results for the threshold quantities are in nice agreement with experimental data and read

$$\begin{aligned}\Delta E - i\Gamma/2 &= +296^{+56}_{-49} - i300^{+42}_{-54} \text{ eV}, \\ \gamma &= +2.44^{+0.73}_{-0.67}, \\ R_n &= +0.268^{+0.110}_{-0.086}, \\ R_c &= +0.643^{+0.015}_{-0.019}.\end{aligned}\tag{6}$$

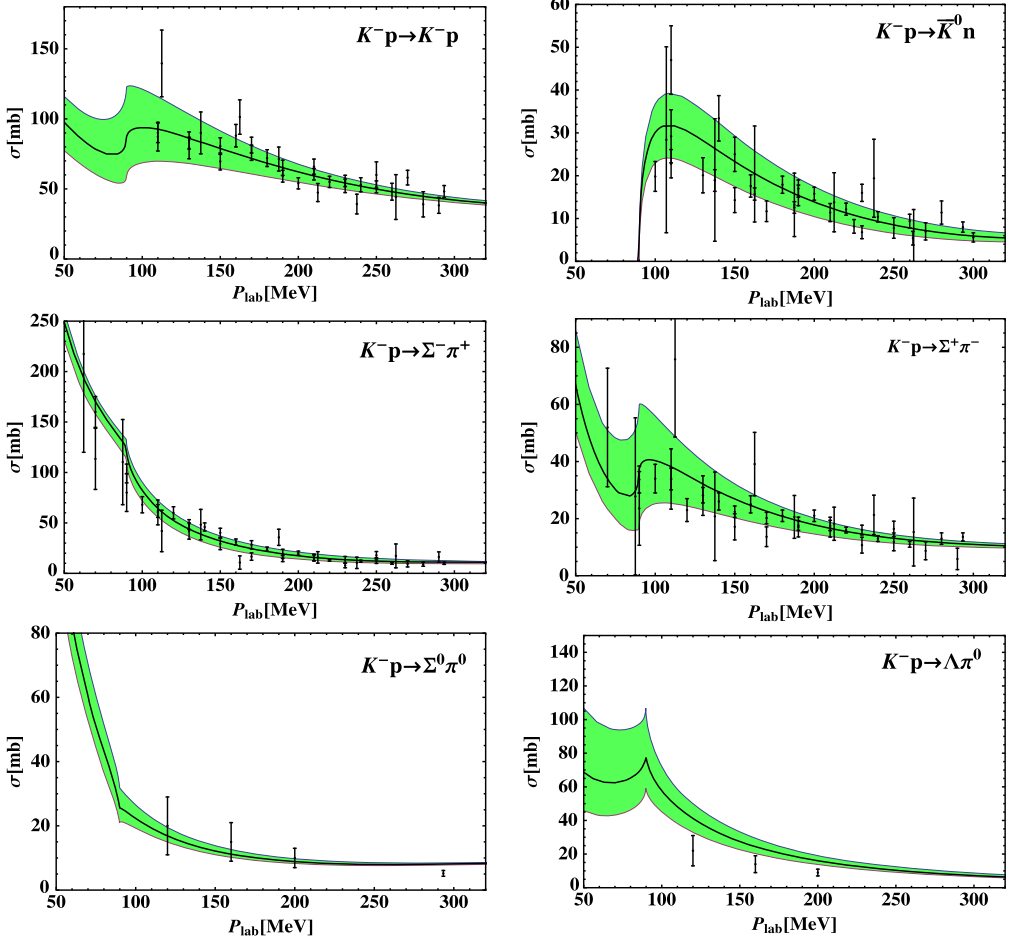


Fig. 1. Total cross sections for the scattering of $K^- p$ to various channels versus the K^- laboratory momentum. The black points with error bars denote the experimental data from [21–24] considered for the fits. The solid (black) lines represent our best fit. Shaded (green in the web version) bands denote the 1σ error bands calculated as described in the text. The reaction $K^- p \rightarrow \Lambda\pi^0$ is not a part of our fit and presented here for completeness.

As a matter of fact, the shape of the 1σ region for the energy shift and width of kaonic hydrogen cannot be assumed to be rectangular, see Fig. 2. The resulting scattering lengths for isospin $I = 0$ and $I = 1$, i.e. a_0 and a_1 , are displayed in Fig. 3, in comparison to some older determinations and the determination based on scattering data alone [5]. The inclusion of the SIDDHARTA data leads to much smaller errors, especially for a_1 . Our values for the scattering lengths are

$$\begin{aligned} a_0 &= -1.81^{+0.30}_{-0.28} + i0.92^{+0.29}_{-0.23} \text{ fm}, \\ a_1 &= +0.48^{+0.12}_{-0.11} + i0.87^{+0.26}_{-0.20} \text{ fm}. \end{aligned} \quad (7)$$

The inclusion of isospin breaking effects was analyzed in [30]. Taking these into account yields: $a_0 = -1.83^{+0.27}_{-0.28} + i0.85^{+0.27}_{-0.22}$ and $a_1 = 0.69^{+0.11}_{-0.12} + i0.95^{+0.31}_{-0.24}$. Note also that the inclusion of the $\Lambda\pi^0$ data in the fitting procedure could yield an additional constraint on the isospin $I = 1$

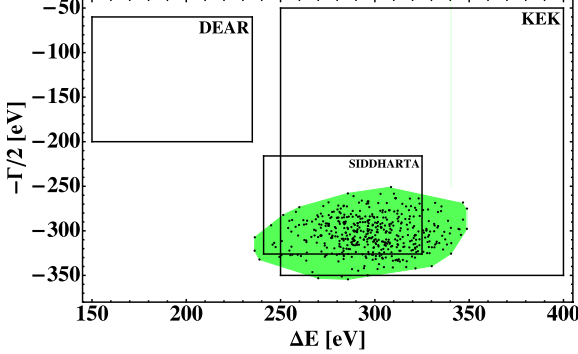


Fig. 2. Energy shift and width of kaonic hydrogen as determined from the DEAR [31], the KEK [32] and the SIDDHARTA [1] experiments. The shaded area denotes the 1σ region of our approach around the best fit value.

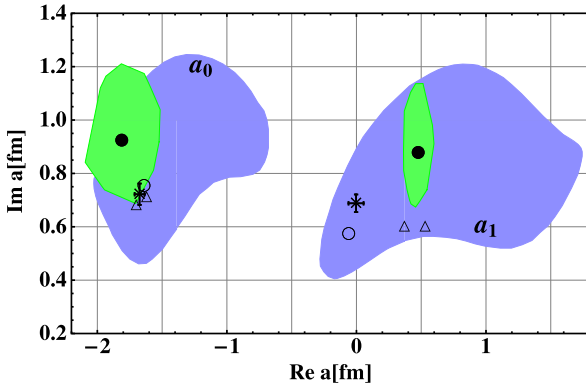


Fig. 3. Real and imaginary part of the isospin $I = 0$ and $I = 1$ $KN \rightarrow KN$ scattering lengths. The light shaded (green in the web version) areas correspond to the 1σ region of our approach around the central value (full circles). The darker (blue in the web version) areas correspond to the 1σ region around central value (empty circle) from Ref. [5] the cross and empty triangles denote older experimental values from [33] and [34], respectively.

amplitudes and fix the value of a_1 as done in [5]. We have not considered this channel as an experimental input for the reasons given above.

The scattering length for the elastic $K^- p$ channel reads

$$a_{K^- p} = -0.68^{+0.18}_{-0.17} + i 0.90^{+0.13}_{-0.13} \text{ fm.} \quad (8)$$

For comparison, taking the SIDDHARTA data only, one obtains $a_{K^- p} = -0.65^{+0.15}_{-0.15} + i 0.81^{+0.18}_{-0.18}$ fm, while Ikeda et al. find² $a_{K^- p} = -0.70^{+0.13}_{-0.13} + i 0.89^{+0.16}_{-0.16}$ fm. Therefore, these fundamental chiral SU(3) parameters can now be considered to be determined with about an accuracy of $\sim 15\%$,

Having fixed the parameters of our model, we can extrapolate the amplitudes of elastic $K^- p$ scattering from the subthreshold region, i.e. center-of-mass energies $1330 \leq W_{\text{cms}} \leq 1450$ MeV. From here on, we concentrate on the s-wave amplitude f_{0+} which is obtained by the standard

² Here, the error bars are extracted from Fig. 4 of [7].

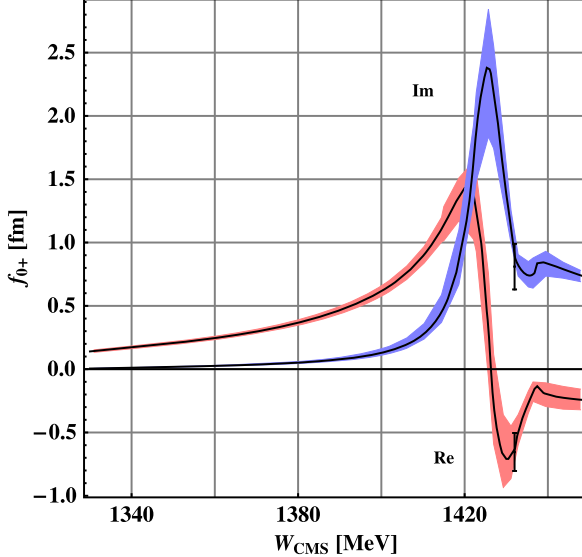


Fig. 4. Real and imaginary part of the s-wave $K^- p \rightarrow K^- p$ scattering amplitude f_{0+} . The shaded band indicates the uncertainty of the calculation. The data point at $W_{\text{cms}} = M_K + m_p$ is determined from the energy shift and width of kaonic hydrogen from the SIDDHARTA experiment.

projection method. The result is presented in Fig. 4. For both real and imaginary parts of the amplitude the maximum lies close to the KN threshold and is quite narrow, which indicates the presence of a close-by pole. It is also worth mentioning that the error band gets smaller to low energies, different to the recent analysis by Ikeda et al. [6,7]. We note that although Ikeda et al. and we describe the scattering and bound state equally well, the subthreshold amplitude is very different. This is presumably due to the different approximation made in these two approaches.

To obtain a more complete picture about the structure of the $\Lambda(1405)$, the amplitudes are analytically continued to the complex W_{cms} plane. Microcausality forbids poles on the first Riemann sheet, that is for $\text{Im}(W_{\text{cms}}) > 0$. This is fulfilled in our model automatically due to the restoration of analyticity as described above. On the other hand, some pole structure has to be responsible for the functional form of the scattering amplitudes $f_{0+}(K^- p \rightarrow K^- p)$, see Fig. 4. Two poles are found on the second Riemann sheet for isospin $I = 0$, which is achieved via analytic continuation to $\text{Im}(W_{\text{cms}}) < 0$. We denote the second Riemann sheet connected to the physical axis in the region between the $\Sigma\pi$ and $\bar{K}N$ threshold as $\mathcal{R}_{\Sigma\pi}$ and the one connected to the physical axis for $W_{\text{cms}} > (M_K + m_N)$ as \mathcal{R}_{KN} . The absolute value of the scattering amplitude is presented on both these sheets in Fig. 5. We find that two poles lie on different Riemann sheets, the corresponding pole positions read

$$\begin{aligned} \mathcal{R}_{\Sigma\pi}: \quad W_1 &= 1428^{+2}_{-1} - i8^{+2}_{-2} \text{ MeV}, \\ \mathcal{R}_{KN}: \quad W_2 &= 1497^{+11}_{-7} - i75^{+9}_{-9} \text{ MeV}. \end{aligned} \quad (9)$$

The real part of the position of the first pole agrees quite well with determination from Refs. [5–7, 13]. Its imaginary part agrees roughly with the determination of Refs. [5, 13] and is significantly smaller than extracted by Ikeda et al. [6,7]. For the second pole, the situation is different, its imaginary part is in agreement with Refs. [5–7], but the real part is much larger. We have analyzed the structure of both resonances utilizing the following representation of the scattering matrix

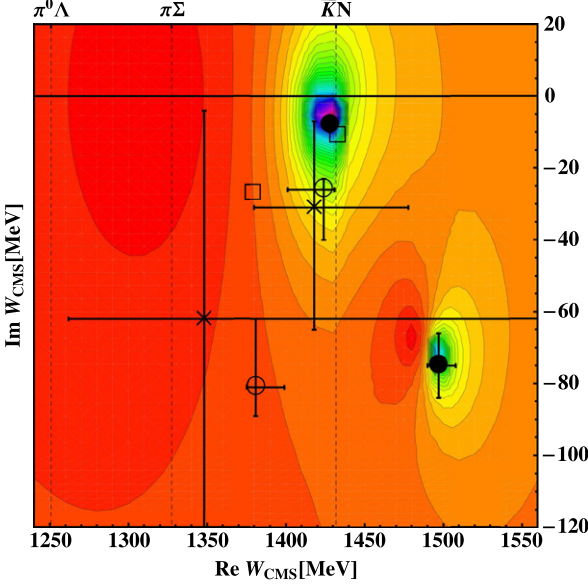


Fig. 5. Contour plot of the absolute value of the scattering amplitude for isospin $I = 0$ in the complex W_{cms} plane. Both Riemann sheets $\mathcal{R}_{\Sigma\pi}$ and $\mathcal{R}_{\bar{K}N}$ are ‘glued’ together along the $\bar{K}N$ threshold line. The pole positions of comparable models are presented in the plot via squares [13], circles [6,7] and crosses [5].

$$T_{ij} \sim \frac{g_i g_j}{s - s_R}, \quad (10)$$

where g_i and g_j are coupling constants of the in- and out-going states, respectively. For each pole (isospin $I = 0$) we extract the coupling constants to the $\bar{K}N$ and $\pi\Sigma$ channel as follows

$$\begin{aligned} W_1: \quad & |g_{\bar{K}N}| = 3.02 \quad \text{and} \quad |g_{\pi\Sigma}| = 1.61, \\ W_2: \quad & |g_{\bar{K}N}| = 1.89 \quad \text{and} \quad |g_{\pi\Sigma}| = 4.39. \end{aligned} \quad (11)$$

At the position of the first pole (the one located at the smaller imaginary value of W_{cms}) the coupling to the $\bar{K}N$ channel is nearly twice as large as to the $\pi\Sigma$ channel. For the second pole this pattern is reversed. Qualitatively both observations agree quite nicely with the ones made in Refs. [4,14].

Having presented the main results of our approach, we wish to comment on differences of our results compared with the outcome of the recent analysis by Ikeda et al. [6,7]. The main observed difference is the different behavior of the $K^- p$ scattering amplitude in the subthreshold energy region which is of course caused by the different pole positions compared to Ikeda et al. We have investigated the origin of these observations qualitatively. First, from the analysis of πN scattering in the same framework, see Ref. [9], it is known that off-shell effects can account for large modifications of the pole positions. Setting the tadpole integrals to zero, we obtain immediately the solution of the BSE in the on-shell factorization. Note that this solution is still different to the one by Ikeda et al. [6,7] since no s-wave projection is performed. Secondly, we noticed much smaller values of the NLO LECs found by Ikeda et al. additionally to the fact that the LECs b_i ($i = 5, \dots, 11$) were neglected there due to the s-wave projection. To keep track of this we scale down our LECs continuously from the values found above to zero. Such a solution of the BSE is of course by no means physical since no further fitting to experimental data is

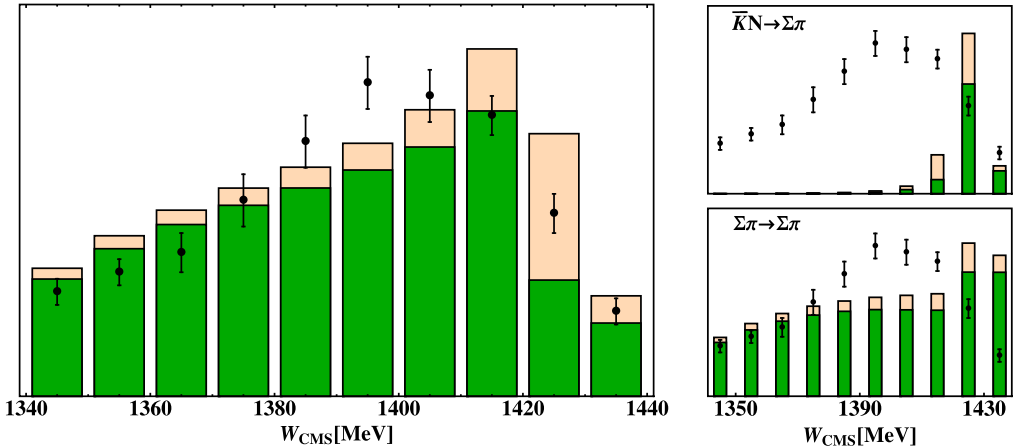


Fig. 6. The prediction of our approach for the $\pi\Sigma$ ($I = 0$) mass distribution (shaded area) as constructed from the $\pi\Sigma \rightarrow \pi\Sigma$ and $\bar{K}N \rightarrow \pi\Sigma$ amplitudes (left figure) in comparison to the experimental data from Ref. [35]. Units are arbitrary and the orange bands represent the uncertainty of our prediction. On the right, the contributions from $\bar{K}N \rightarrow \pi\Sigma$ and $\pi\Sigma \rightarrow \pi\Sigma$ channels are presented separately.

done here. Qualitatively, however, we observe that both poles move (the second one by about 100 MeV) to lower values of $\text{Re}(W_{\text{cms}})$. The conclusion to be drawn is that the s-wave projection in the on-shell approximation of the interaction kernel is the main reason³ for the difference in pole positions extracted in Ikeda et al. compared to those extracted from our approach.

Finally, we have calculated the $\pi\Sigma$ mass distribution from the reaction $\Sigma^+(1660) \rightarrow \pi^+(\pi^-\Sigma^+)$ [35]. Similar to the analysis of Ref. [13], we have calculated a linear combination $(xT_{\bar{K}N \rightarrow \pi\Sigma} + yT_{\pi\Sigma \rightarrow \pi\Sigma})$ with unknown parameters x and y . Then, this combination is squared and multiplied with the three-body phase space factor times a free unknown parameter z . All three parameters are adjusted to reproduce the data from Ref. [35] as presented in Fig. 6. The actual values are: $x = -0.858$, $y = 0.933 - i0.235$, and $z = 14.55$. Thus, despite the differences described before, the experimental data is described rather well and is of similar quality as the one obtained by Ikeda et al. Clearly, we do not describe the latter perfectly, but by no means this can be taken as a decisive argument against our solution, as e.g. the extraction of this mass distribution is not free of any model-dependence. It will be of utmost importance to work out the recently measured precise $\pi\Sigma$ distributions obtained from photoproduction experiments at Jefferson Lab [36] (see also [37]) and also more modern hadronic data from COSY [38] and HADES [39].

Acknowledgements

We are grateful to Peter Bruns and Michael Döring for their stimulating remarks and cooperation. We thank Wolfram Weise for comments. This work is supported in part by the DFG (SFB/TR 16 “Subnuclear Structure of Matter”) and by the EU HadronPhysics3 project “Study of Strongly Interacting Matter”.

³ The influence of the Born graphs is not addressed in the present discussion as they cannot be included in our off-shell framework as mentioned before.

Appendix A. Couplings

For the channel indices $\{b, j; i, a\}$ corresponding to the process $\phi_i B_a \rightarrow \phi_j B_b$ the relevant coupling matrices read

$$\begin{aligned}
A_{WT}^{b,j;i,a} &= -\frac{1}{4F_j F_i} \langle \lambda^{b\dagger} [[\lambda^{j\dagger}, \lambda^i], \lambda^a] \rangle, \\
A_{14}^{b,j;i,a} &= -\frac{2}{F_j F_i} (b_1 (\langle \lambda^{b\dagger} [\lambda^{j\dagger}, [\lambda^i, \lambda^a]] \rangle + \langle \lambda^{b\dagger} [\lambda^i, [\lambda^{j\dagger}, \lambda^a]] \rangle) \\
&\quad + b_2 (\langle \lambda^{b\dagger} \{\lambda^{j\dagger}, [\lambda^i, \lambda^a]\} \rangle + \langle \lambda^{b\dagger} \{\lambda^i, [\lambda^{j\dagger}, \lambda^a]\} \rangle) \\
&\quad + b_3 (\langle \lambda^{b\dagger} \{\lambda^{j\dagger}, \{\lambda^i, \lambda^a\}\} \rangle + \langle \lambda^{b\dagger} \{\lambda^i, \{\lambda^{j\dagger}, \lambda^a\}\} \rangle) + 2b_4 \langle \lambda^{b\dagger} \lambda^a \rangle \langle \lambda^{j\dagger} \lambda^i \rangle), \\
A_{57}^{b,j;i,a} &= -\frac{2}{F_j F_i} (b_5 (\langle \lambda^{b\dagger} [[\lambda^{j\dagger}, \lambda^i], \lambda^a] \rangle + b_6 \langle \lambda^{b\dagger} \{[\lambda^{j\dagger}, \lambda^i], \lambda^a\} \rangle \\
&\quad + b_7 (\langle \lambda^{b\dagger} \lambda^{j\dagger} \rangle \langle \lambda^i \lambda^a \rangle + \langle \lambda^{b\dagger} \lambda^i \rangle \langle \lambda^a \lambda^{j\dagger} \rangle)), \\
A_{811}^{b,j;i,a} &= -\frac{1}{F_j F_i} (b_8 (\langle \lambda^{b\dagger} [\lambda^{j\dagger}, [\lambda^i, \lambda^a]] \rangle + \langle \lambda^{b\dagger} [\lambda^i, [\lambda^{j\dagger}, \lambda^a]] \rangle) \\
&\quad + b_9 (\langle \lambda^{b\dagger} [\lambda^{j\dagger}, \{\lambda^i, \lambda^a\}] \rangle + \langle \lambda^{b\dagger} [\lambda^i, \{\lambda^{j\dagger}, \lambda^a\}] \rangle) \\
&\quad + b_{10} (\langle \lambda^{b\dagger} \{\lambda^{j\dagger}, \{\lambda^i, \lambda^a\}\} \rangle + \langle \lambda^{b\dagger} \{\lambda^i, \{\lambda^{j\dagger}, \lambda^a\}\} \rangle) + 2b_{11} \langle \lambda^{b\dagger} \lambda^a \rangle \langle \lambda^{j\dagger} \lambda^i \rangle), \\
A_M^{b,j;i,a} &= -\frac{1}{2F_j F_i} (2b_0 \langle \lambda^{b\dagger} \lambda^a \rangle \langle [\lambda^{j\dagger} \lambda^i] \bar{\mathcal{M}} \rangle + b_D (\langle \lambda^{b\dagger} \{[\lambda^{j\dagger}, \{\bar{\mathcal{M}}, \lambda^i\}], \lambda^a \} \rangle \\
&\quad + \langle \lambda^{b\dagger} \{[\lambda^i, \{\bar{\mathcal{M}}, \lambda^{j\dagger}\}], \lambda^a \} \rangle) + b_F (\langle \lambda^{b\dagger} \{[\lambda^{j\dagger}, \{\bar{\mathcal{M}}, \lambda^i\}], \lambda^a \} \rangle \\
&\quad + \langle \lambda^{b\dagger} \{[\lambda^i, \{\bar{\mathcal{M}}, \lambda^{j\dagger}\}], \lambda^a \} \rangle)),
\end{aligned}$$

where λ denote the 3×3 channel matrices (e.g. $\phi = \phi^i \lambda^i$ for the physical meson fields) and the F_i are the meson decay constants in the respective channel. Moreover, $\bar{\mathcal{M}}$ is obtained from the quark mass matrix \mathcal{M} via the Gell-Mann–Oakes–Renner relations, and given in terms of the meson masses as follows, $\bar{\mathcal{M}} = \frac{1}{2} \text{diag}(M_{K^+}^2 - M_{K^0}^2 + M_{\pi^0}^2, M_{K^0}^2 - M_{K^+}^2 + M_{\pi^0}^2, M_{K^+}^2 + M_{K^0}^2 - M_{\pi^0}^2)$.

References

- [1] M. Bazzi, et al., Phys. Lett. B 704 (2011) 113, arXiv:1105.3090 [nucl-ex];
M. Bazzi, G. Beer, L. Bombelli, A.M. Bragadireanu, M. Cargnelli, G. Corradi, C. Curceanu (Petrascu), A. d’Uffizi, et al., Nucl. Phys. A 881 (2012) 88, arXiv:1201.4635 [nucl-ex].
- [2] R.H. Dalitz, S.F. Tuan, Annals Phys. 10 (1960) 307.
- [3] B. Borasoy, R. Nißler, W. Weise, Eur. Phys. J. A 25 (2005) 79, hep-ph/0505239.
- [4] J.A. Oller, Eur. Phys. J. A 28 (2006) 63, hep-ph/0603134.
- [5] B. Borasoy, U.-G. Meißner, R. Nißler, Phys. Rev. C 74 (2006) 055201, hep-ph/0606108.
- [6] Y. Ikeda, T. Hyodo, W. Weise, Phys. Lett. B 706 (2011) 63, arXiv:1109.3005 [nucl-th].
- [7] Y. Ikeda, T. Hyodo, W. Weise, Nucl. Phys. A 881 (2012) 98, arXiv:1201.6549 [nucl-th].
- [8] Z.-H. Guo, J.A. Oller, arXiv:1210.3485 [hep-ph].
- [9] P.C. Bruns, M. Mai, U.-G. Meißner, Phys. Lett. B 697 (2011) 254, arXiv:1012.2233 [nucl-th].
- [10] M. Mai, P.C. Bruns, U.-G. Meißner, Phys. Rev. D 86 (2012) 094033, arXiv:1207.4923 [nucl-th].
- [11] M. Döring, U.-G. Meißner, Phys. Lett. B 704 (2011) 663, arXiv:1108.5912 [nucl-th].
- [12] N.V. Shevchenko, Nucl. Phys. A 890–891 (2012) 50, arXiv:1201.3173 [nucl-th].
- [13] J.A. Oller, U.-G. Meißner, Phys. Lett. B 500 (2001) 263, hep-ph/0011146.
- [14] D. Jido, J.A. Oller, E. Oset, A. Ramos, U.-G. Meißner, Nucl. Phys. A 725 (2003) 181, nucl-th/0303062.

- [15] A. Krause, Helv. Phys. Acta 63 (1990) 3.
- [16] M. Frink, U.-G. Meißner, JHEP 0407 (2004) 028, hep-lat/0404018.
- [17] Y.-R. Liu, S.-L. Zhu, Phys. Rev. D 75 (2007) 034003, hep-ph/0607100.
- [18] M. Mai, P.C. Bruns, B. Kubis, U.-G. Meißner, Phys. Rev. D 80 (2009) 094006, arXiv:0905.2810 [hep-ph].
- [19] N. Kaiser, Phys. Rev. C 64 (2001) 045204, nucl-th/0107006;
N. Kaiser, Phys. Rev. C 73 (2006) 069902 (Erratum).
- [20] E.E. Salpeter, H.A. Bethe, Phys. Rev. 84 (1951) 1232.
- [21] J. Ciborowski, et al., J. Phys. G 8 (1982) 13.
- [22] W.E. Humphrey, R.R. Ross, Phys. Rev. 127 (1962) 1305.
- [23] M. Sakitt, T.B. Day, R.G. Glasser, N. Seeman, J.H. Friedman, W.E. Humphrey, R.R. Ross, Phys. Rev. 139 (1965) B719.
- [24] M.B. Watson, M. Ferro-Luzzi, R.D. Tripp, Phys. Rev. 131 (1963) 2248.
- [25] D.N. Tovee, et al., Nucl. Phys. B 33 (1971) 493.
- [26] R.J. Nowak, et al., Nucl. Phys. B 139 (1978) 61.
- [27] J.K. Kim, Phys. Rev. Lett. 19 (1967) 1074.
- [28] U.-G. Meißner, U. Raha, A. Rusetsky, Eur. Phys. J. C 35 (2004) 349, hep-ph/0402261.
- [29] Minuit2 released in ROOT 5.22/00, <http://lcgapp.cern.ch/project/cls/work-packages/mathlibs/minuit>.
- [30] U.-G. Meißner, U. Raha, A. Rusetsky, Eur. Phys. J. C 47 (2006) 473, nucl-th/0603029.
- [31] G. Beer, et al., DEAR Collaboration, Phys. Rev. Lett. 94 (2005) 212302.
- [32] T.M. Ito, et al., Phys. Rev. C 58 (1998) 2366.
- [33] J.K. Kim, Phys. Rev. Lett. 14 (1965) 29.
- [34] A.D. Martin, Nucl. Phys. B 179 (1981) 33.
- [35] R.J. Hemingway, Nucl. Phys. B 253 (1985) 742.
- [36] K. Moriya, et al., CLAS Collaboration, Nucl. Phys. A 835 (2010) 325, arXiv:0911.2705 [nucl-ex];
K. Moriya, et al., CLAS Collaboration, arXiv:1301.5000 [nucl-ex].
- [37] M. Niiyama, H. Fujimura, D.S. Ahn, J.K. Ahn, S. Ajimura, H.C. Bhang, T.H. Chang, W.C. Chang, et al., Phys. Rev. C 78 (2008) 035202, arXiv:0805.4051 [hep-ex].
- [38] I. Zychor, M. Buscher, M. Hartmann, A. Kacharava, I. Keshelashvili, A. Khoukaz, V. Kleber, V. Koptev, et al., Phys. Lett. B 660 (2008) 167, arXiv:0705.1039 [nucl-ex].
- [39] G. Agakishiev, A. Balanda, D. Belver, A.V. Belyaev, J.C. Berger-Chen, A. Blanco, M. Bohmer, J.L. Boyard, et al., arXiv:1208.0205 [nucl-ex].